

Estimating the concentration of total suspended solids in inland and coastal waters from Sentinel-2 MSI: A semi-analytical approach

Dalin Jiang ^{a,*}, Bunkei Matsushita ^b, Nima Pahlevan ^{c,d}, Daniela Gurlin ^e, Cédric G. Fichot ^f, Joshua Harringmeyer ^f, Giulia Sent ^g, Ana C. Brito ^{g,h}, Vanda Brotas ^{g,h}, Mortimer Werther ⁱ, Veloisa Mascarenhas ^a, Matthew Blake ^a, Peter Hunter ^a, Andrew Tyler ^a, Evangelos Spyarakos ^a

^a Earth and Planetary Observation Sciences (EPOS), Biological and Environmental Sciences, Faculty of Natural Sciences, University of Stirling, Stirling, United Kingdom

^b Faculty of Life and Environmental Sciences, University of Tsukuba, Ibaraki, Japan

^c NASA Goddard Space Flight Center, Greenbelt, MD, USA

^d Science Systems and Applications Inc. (SSAI), Lanham, MD, USA

^e Wisconsin Department of Natural Resources, Madison, WI, USA

^f Department of Earth and Environment, Boston University, Boston, MA, USA

^g MARE-Marine and Environmental Science Centre/ARNET-Aquatic Research NETwork, Faculdade de Ciências da Universidade de Lisboa, 1749-016 Lisboa, Portugal

^h Departamento de Biología Vegetal, Faculdade de Ciências, Universidade de Lisboa, Campo Grande, 1749-016 Lisboa, Portugal

ⁱ Swiss Federal Institute of Aquatic Science and Technology, Department of Surface Waters - Research and Management, Dübendorf, Switzerland

ARTICLE INFO

Keywords:

Total suspended solids
Semi-analytical algorithm
Sentinel-2 MSI
Inland waters
Coastal waters

ABSTRACT

Inland and coastal waters provide key ecosystem services and are closely linked to human well-being. In this study, we propose a semi-analytical method, which can be applied to Sentinel-2 MultiSpectral Instrument (MSI) images to retrieve high spatial-resolution total suspended solids (TSS) concentration in a broad spectrum of aquatic ecosystems ranging from clear to extremely turbid waters. The presented approach has four main steps. First, the remote sensing reflectance (R_s) at a band lacking in MSI (620 nm) is estimated through an empirical relationship from R_s at 665 nm. Second, waters are classified into four types (clear, moderately turbid, highly turbid, and extremely turbid). Third, semi-analytical algorithms are used to estimate the particulate backscattering coefficient (b_{bp}) at a reference band depending on the water types. Last, TSS is estimated from b_{bp} at the reference band. Validation and comparison of the proposed method with three existing methods are performed using a simulated dataset ($N = 1000$), an *in situ* dataset collected from global inland and coastal waters ($N = 1265$) and satellite matchups ($N = 40$). Results indicate that the proposed method can improve TSS estimation and provide accurate retrievals of TSS from all three datasets, with a median absolute percentage error (MAPE) of 14.88 %, 31.50 % and 41.69 % respectively. We also present comparisons of TSS mapping between the Sentinel-3 Ocean and Land Colour Instrument (OLCI) and MSI in Lake Kasumigaura, Japan and the Tagus Estuary, Portugal. Results clearly demonstrate the advantages of using MSI for TSS monitoring in small water bodies such as rivers, river mouths and other nearshore waters. MSI can provide more detailed and realistic TSS estimates than OLCI in these water bodies. The proposed TSS estimation method was applied to MSI images to produce TSS time-series in Lake Kasumigaura, which showed good agreements with *in situ* and OLCI-derived TSS time-series.

1. Introduction

Over half of the global population live within 3 km of a fresh water body (Kummu et al., 2011), while 23 % live in coastal zones (Small & Nicholls, 2003). Inland and coastal waters provide fundamental ecosystem services such as drinking water provision, fisheries, biodiversity conservation, irrigation water provision, transportation,

electricity production, recreation and tourism (Schallenberg et al., 2013; Reynaud & Lanzanova, 2017; Sterner et al., 2020; Heino et al., 2021). Efficient water quality monitoring of inland and coastal waters is required to support water management and decision-making to ensure the sustainable use of these resources.

Ocean colour sensors, such as the Medium Resolution Imaging Spectrometer (MERIS) and Ocean and Land Colour Instrument (OLCI)

* Corresponding author.

E-mail address: dalin.jiang@stir.ac.uk (D. Jiang).

with a spatial resolution of 300 m, and the Moderate Resolution Imaging Spectroradiometer (MODIS) with a spatial resolution of 1000 m, have been widely used to monitor water quality in relatively large lakes and coastal waters (Gons et al., 2008; Binding et al., 2012; Vundo et al., 2019; Jiang et al., 2019; Shen et al., 2020). However, 99 % of the approximately 117 million lakes on Earth are smaller than 1 km², covering ~40 % of the global lake area (Verpoorter et al., 2014). This large number of small lakes highlights that most global lakes are difficult to monitor using medium resolution satellite images such as the ones acquired from MERIS and OLCI, given that at least nine pixels ($0.3 \text{ km} \times 0.3 \text{ km} \times 9 = 0.81 \text{ km}^2$) are required (Verpoorter et al., 2014). Furthermore, small bays, lagoons, and estuaries, where water quality can vary on a spatial scale of tens of metres, can be particularly challenging to observe adequately with these sensors. Given the limitations of using medium-resolution satellite data for water quality monitoring in small inland and coastal water bodies, it is imperative to explore solutions using higher spatial resolution satellite data. The MultiSpectral Instrument (MSI) onboard Sentinel-2 has 13 spectral bands with high spatial resolution of up to 10 m. The constellation of two satellites (Sentinel-2A and 2B) has shortened the revisit period to five days at the equator (Drusch et al., 2012). The high spatial and temporal resolution of MSI makes it a suitable candidate for inland and coastal water monitoring (Pahlevan et al., 2017; Warren et al., 2019).

The concentration of total suspended solids (TSS), which influences the water transparency and light availability in the water column (Brown, 1984; McCullough & Barber, 2007), is a key water quality indicator used in monitoring activities. However, there is limited research on the TSS retrieval capabilities using MSI imagery for inland and coastal waters. Although several empirical methods were developed to retrieve TSS from MSI images (Liu et al., 2017; Li et al., 2019; Ciancia et al., 2020), their applicability to waters with different inherent optical properties (IOPs) is often limited due to the specific conditions for which they were developed. Existing semi-analytical approaches for retrieving TSS from MSI imagery can also be limited by the range of data used to calibrate these models (Nechad et al., 2010; Han et al., 2016). For example, the semi-analytical method developed by Nechad et al. (2010) can be applied to MSI images, but it was developed for turbid waters and is not appropriate for clear waters. Other research includes the use of machine learning (ML) methods to estimate TSS from MSI images (Saberoon et al., 2020; Balasubramanian et al., 2020; Pahlevan et al., 2022), but the generalisation ability of ML methods depends on the dataset used for model training. Considering the bio-optical complexity of inland and coastal waters, it is desirable to use a semi-analytical method which is applicable for clear to extremely turbid water types and does not require recalibration or coefficient tuning.

Recently, Jiang et al. (2021) developed a semi-analytical method that estimates TSS from the particulate backscattering coefficient (b_{bp}) at four different bands for clear to extremely turbid waters based on a water type classification. This method was evaluated using a simulated dataset (TSS range 0.01–1100 g/m³) and an *in situ* dataset collected from global lakes and coastal waters (TSS range 0.09–2627 g/m³), and it outperformed other existing methods (Jiang et al., 2021; Tan et al., 2022). However, applying the approach by Jiang et al. (2021) to MSI imagery presents two main challenges. Firstly, the band at 620 nm, which is required for the water type classification, is not available on the MSI sensor. Secondly, the method was originally designed for MERIS and OLCI sensors, thereby necessitating adaptation of the algorithm to the MSI bands because bandwidths and band centres are different.

Consequently, the objectives of this study are to: (1) develop a semi-analytical method for MSI imagery to accurately estimate TSS across a range of water optical conditions; (2) validate the proposed TSS estimation method using simulated data, *in situ* data and satellite matchups; and (3) assess the potential of MSI for monitoring TSS in inland and coastal waters.

2. Data acquisition

2.1. In situ data collection

We collected 1265 *in situ* remote sensing reflectance (R_{rs}) and corresponding TSS measurements from 69 lakes in Japan, Indonesia, China, USA, Switzerland, Sweden, UK and Italy, and 11 coastal waters (including rivers) in Japan, Indonesia, Germany, France, Argentina, Belgium, USA and Portugal (Fig. 1). The *in situ* TSS covers a wide range from 0.1 g/m³ to 1400 g/m³ with a median value of 9.9 g/m³ (Fig. 1a). R_{rs} spectra were measured using either in-water ($N = 478$) or above-water approaches ($N = 767$). Using the in-water method, the upwelling radiance below the water surface (L_u^{0-}) and downwelling irradiance (E_d^{0+}) were measured with a pair of intercalibrated miniature fibre optic spectrometers. Water-leaving radiance (L_w) was obtained by correcting for the air–water interface effects assuming a constant upward Fresnel transmittance of the air–water interface of ~0.975 (Mueller et al., 2003), and a water temperature and wavelength specific refractive index of water (Quan and Fry, 1995), and R_{rs} was calculated as L_w/E_d^{0+} (Gurlin et al., 2011). In the above-water approach, the total radiance from the water surface (L_t), sky radiance (L_s) and E_d^{0+} were measured, and R_{rs} was calculated as $(L_t - \rho L_s)/E_d^{0+}$, where ρ is the water surface reflectance factor (Mobley, 1999). In addition, we obtained 20 R_{rs} spectra from airborne imagery collected with the Portable Remote Imaging SpectroMeter (PRISM) at ~6 km altitude (Fichot et al., 2016). Finally, the residual reflected skylight effects were removed from all above-water measured R_{rs} using the method proposed from Jiang et al. (2020). All *in situ* R_{rs} were convolved to Sentinel-2 MSI bands using the MSI spectral response functions. These 1265 *in situ* R_{rs} -TSS pairs were used to develop the model for estimating R_{rs} at 620 nm, and validate the proposed TSS method.

We also used monthly *in situ* TSS data from seven stations at Lake Kasumigaura (Fig. 1b), which is a turbid shallow lake with an average depth of 4 m and a surface area of 171 km² (Oyama et al., 2009), representing the period of 2015–2020 to evaluate the TSS time-series estimated from satellite images. Those *in situ* TSS data were collected from the National Institute for Environmental Studies, Japan (NIES, 2020). In addition, typhoon information including location and time, meteorological data including wind speed and precipitation at the Tsuchiura meteorological station (nearshore of Lake Kasumigaura) were also collected from the Japan Meteorological Agency (JMA, <https://www.jma.go.jp>) and used to study the causes of high TSS events observed in Lake Kasumigaura.

2.2. Synthetic data generation

Two synthetic datasets were used in this study. Synthetic Dataset I includes 1,171,875 TSS and TSS-specific particulate backscattering coefficient (b_{bp}^*) pairs in 1 nm intervals. The simulated Chl-a concentration ranges from 0.01 mg/m³ to 1000 mg/m³, and tripton ranges from 0.01 g/m³ to 1000 g/m³. Synthetic Dataset I was used to recalibrate the coefficient of b_{bp}^* for MSI bands. Synthetic Dataset II includes 1000 R_{rs} -TSS pairs with the TSS ranging from 0.01 g/m³ to 1100 g/m³, which were simulated based on a bio-optical model. Synthetic Dataset II was used to validate the developed TSS method. Details describing the equations and parameters for the two synthetic dataset simulations can be found in Jiang et al. (2021; Synthetic Dataset I and III in that work).

2.3. Satellite data acquisition and processing

We downloaded 17 Sentinel-2 MSI Level-1C satellite images over lakes Kasumigaura and Hibara in Japan, Lake Poygan and the Plum Island Estuary in the USA, Loch Lomond in the UK, Lake Garda in Italy, and the Tagus Estuary in Portugal from USGS (<https://earthexplorer.usgs.gov>). These satellite images were used to validate the TSS

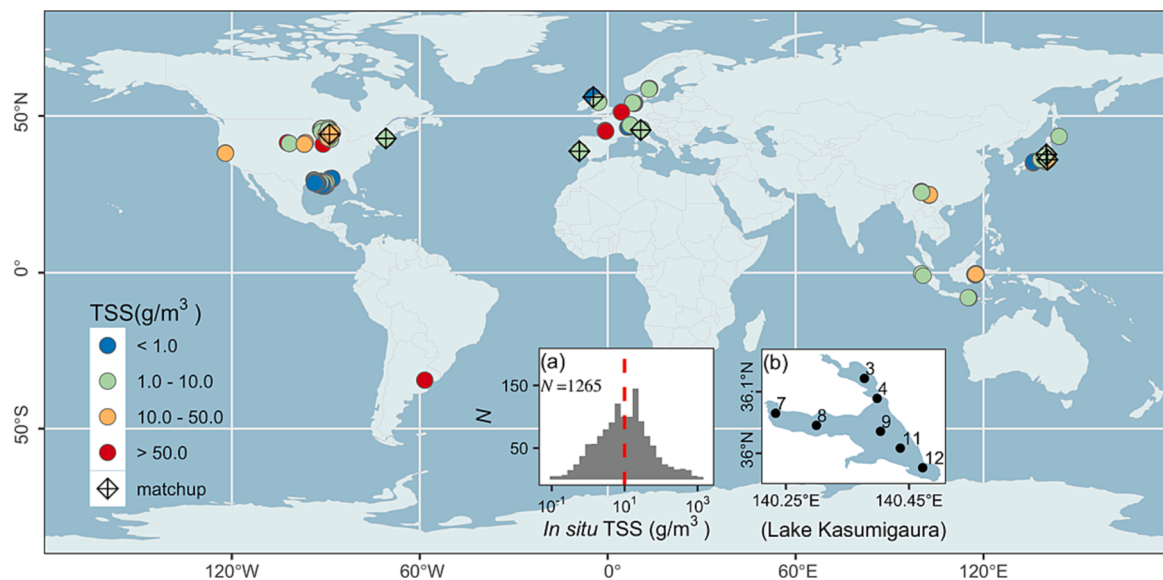


Fig. 1. Location of *in situ* data used in this study, diamond plus symbol indicates the location of satellite matchups. (a) Histogram of *in situ* TSS, red dashed line indicates the median value. (b) Routine monitoring sites in Lake Kasumigaura (Japan).

estimation method for satellite matchups (Table 1).

We also downloaded 314 Level-1C MSI images acquired over Lake Kasumigaura from 2015 to 2020 to produce a MSI-based TSS time-series derived with the TSS method proposed in this study. In addition, we downloaded 674 Sentinel-3 OLCI Level-1 images acquired over Lake Kasumigaura from 2016 to 2020 to produce an OLCI-based TSS time-series using the method of Jiang et al. (2021). The two time-series datasets were used to explore the consistency of TSS monitoring between MSI and OLCI. One MSI and one OLCI image acquired over the Tagus Estuary on 19 October 2021 were also included in this study to demonstrate the differences in TSS monitoring with the different spatial resolutions between OLCI and MSI.

The Case 2 Regional Coast Colour (C2RCC) processor in the Sentinel Application Platform (SNAP) version 8.0 was used for atmospheric correction of MSI and OLCI Level-1 products. Clouds and cloud shadows were identified and removed using the IdePix module in SNAP. All MSI images in this study were resampled at a 20 m × 20 m spatial resolution. The average TSS in a 3 × 3-pixel window was extracted and compared with *in situ* TSS, and produced the TSS time-series. Satellite matchups were defined as that *in situ* data collected within one hour of satellite overpass. In total, we obtained 40 MSI matchups (Table 1), which were then used for the proposed TSS estimation method validation.

3. Algorithm development

3.1. TSS estimation algorithm

TSS can be estimated from the particulate backscattering coefficient and TSS-specific particulate backscattering coefficient following the equation by Nechad et al. (2010) and Jiang et al. (2021):

$$\text{TSS} = \frac{1}{b_{bp}^*(\lambda)} b_{bp}(\lambda) \quad (1)$$

where b_{bp}^* can be obtained from simulations, b_{bp} can be estimated from R_{rs} , and λ denotes the wavelength used for TSS estimation. The response of R_{rs} to changes in TSS varies across wavelengths depending on the water turbidity. For example, R_{rs} at short wavelengths (e.g., blue, green) are sensitive to TSS variations in clear waters, but they may become saturated in extremely turbid waters. In these turbid waters, R_{rs} at a longer wavelength (e.g., in the red or near-infrared (NIR)) is more sensitive to changes in TSS than at shorter wavelengths (Knaeps et al., 2015; Novoa et al., 2017). This characteristic suggests that accurate estimation of TSS requires the use of an appropriate reference band that is sensitive to TSS changes and necessitates employing different wavelengths for different types of water.

b_{bp} can be calculated using the quasi-analytical algorithm (QAA; Lee et al., 2002) as follows:

$$r_{rs}(\lambda) = \frac{R_{rs}(\lambda)}{0.52 + 1.7R_{rs}(\lambda)} \quad (2)$$

$$u(\lambda) = \frac{-0.089 + \sqrt{0.089^2 + 4 \times 0.125 \times r_{rs}(\lambda)}}{2 \times 0.125} \quad (3)$$

$$a(\lambda_0) = a_w(\lambda_0) + \Delta a(\lambda_0) \quad (4)$$

$$b_{bp}(\lambda_0) = \frac{u(\lambda_0) \times a(\lambda_0)}{1 - u(\lambda_0)} - b_{bw}(\lambda_0) \quad (5)$$

where $a(\lambda_0)$ is the total absorption coefficient at a reference band (λ_0), $\Delta a(\lambda_0)$ is the absorption coefficient contributed by optically active components at the reference band, $b_{bp}(\lambda_0)$ is the backscattering coefficient at the reference band and finally used for TSS estimation. a_w is the absorption coefficient of pure water (Kou et al., 1993; Pope and Fry,

Table 1
TSS matchups used in this study.

Location	Date (YYYY/MM/DD)	Number of matchups
Lake Kasumigaura, Japan	2016/10/27, 2016/11/29, 2018/01/10, 2018/02/07, 2018/10/10, 2019/05/08	16
Lake Hibara, Japan	2018/06/02	4
Lake Poygan, USA	2018/09/11	1
Plum Island Estuary, USA	2018/06/12, 2018/07/19, 2022/10/06, 2022/10/19	11
Lake Garda, Italy	2017/03/08, 2017/09/21	2
Loch Lomond, UK	2016/08/24, 2017/08/09	4
Tagus Estuary, Portugal	2021/10/19	2
In total		40

1997), and b_{bw} is the backscattering coefficient of pure water (Zhang et al., 2009). The crucial step of the b_{bp} calculation is the accurate estimation of $a(\lambda_0)$. It has been proposed that if an appropriate wavelength is chosen, where the total absorption (a) is dominated by a_w , then we can assume $a \approx a_w$, and the contribution by Δa in the estimation of a is limited (Lee et al., 2002). For example, $\lambda_0=560$ nm can be chosen for clear waters, but it will not work for turbid waters as the increase of particles will greatly increase the value of Δa , hence the assumption of $a \approx a_w$ will no longer be valid, and a reference band in the red or NIR is required.

An appropriate reference band should therefore be selected so that $R_{rs}(\lambda_0)$ is sensitive to TSS variation and the assumption for $a(\lambda_0) \approx a_w(\lambda_0)$ also holds. To address these two considerations, waters can be classified into four types (Fig. 2): clear water (water type I), moderately turbid water (water type II), highly turbid water (water type III) and extremely turbid water (water type IV) by comparing R_{rs} at 490 nm, 560 nm, 620 nm and 740 nm (Jiang et al. 2021).

For water type I, the band at 560 nm can be chosen as the reference band, and the absorption coefficient at 560 nm can be estimated using (Lee et al., 2009):

$$a(560) = a_w(560) + 10^{-1.146 - 1.366x - 0.469x^2}, \quad (6)$$

$$x = \log \left(\frac{r_{rs}(443) + r_{rs}(490)}{r_{rs}(560) + 5 \frac{r_{rs}(665)}{r_{rs}(490)} r_{rs}(665)} \right) \quad (7)$$

For water type II, the band at 665 nm can be chosen as the reference band, and the absorption coefficient at 665 nm can be estimated through (IOCCG, 2014):

$$a(665) = a_w(665) + 0.39 \left(\frac{R_{rs}(665)}{R_{rs}(443) + R_{rs}(490)} \right)^{1.14} \quad (8)$$

For water type III, the band at 740 nm can be chosen as the reference band, because a_w at 740 nm is high (2.7 m^{-1} , Kou et al., 1993) and it is assumed that:

$$a(740) \approx a_w(740) \quad (9)$$

For water type IV, the band at 865 nm can be chosen as the reference band, because a_w at 865 nm reaches 4.6 m^{-1} (Kou et al., 1993), thus we can assume that:

$$a(865) \approx a_w(865) \quad (10)$$

However, two problems emerge when attempting to apply this TSS retrieval approach to MSI: first, R_{rs} at 620 nm is necessary for water type classification (Fig. 2), but is not available from MSI; second, because the band centres and widths are different between MSI and MERIS (and OLCI), it is necessary to recalibrate the coefficient of b_{bp}^* for use with MSI. We therefore propose a model to estimate $R_{rs}(620)$, and recalibrate b_{bp}^* for MSI in this study.

3.2. Algorithm and parameter re-tuning for TSS estimation from MSI

We chose $R_{rs}(665)$ to estimate $R_{rs}(620)$ in this study, because it is the closest band on MSI. We built an empirical relationship to estimate $R_{rs}(620)$ from $R_{rs}(665)$ using the *in situ* Dataset ($N = 1265$, Fig. 3). When $R_{rs}(665)$ has values between 0 and 0.02 sr^{-1} , $R_{rs}(665)$ is generally lower than $R_{rs}(620)$. When $R_{rs}(665)$ spans between 0.02 and 0.04 sr^{-1} , $R_{rs}(665)$ is generally similar to $R_{rs}(620)$. When $R_{rs}(665)$ is higher than $\sim 0.04 \text{ sr}^{-1}$, $R_{rs}(665)$ is generally higher than $R_{rs}(620)$. This characteristic indicates that for clearer waters, R_{rs} decreases from short to longer wavelengths, and when water is extremely turbid, R_{rs} at long wavelengths (such as red and NIR) will be higher than at short wavelengths because of high suspended solids or phytoplankton. Therefore, to model the relationship between $R_{rs}(620)$ and $R_{rs}(665)$, we fitted a third-order polynomial to the data and derived the following equation:

$$R_{rs}(620) = 169.385R_{rs}(665)^3 - 15.576R_{rs}(665)^2 + 1.317R_{rs}(665) + 0.000148 \quad (11)$$

We convoluted the original simulated 1 nm b_{bp}^* data (Synthetic Dataset I, $N = 1,171,875$) using the MSI spectral response functions to optimise the b_{bp}^* for MSI. The median $1/b_{bp}^*$ values at MSI bands shown in Table 2 were finally used to estimate TSS from MSI.

To summarise, the TSS estimation method proposed in this study for MSI includes four main steps: (1) estimate $R_{rs}(620)$ from $R_{rs}(665)$ using Eq. (11); (2) classify water types as shown in Fig. 2; (3) estimate b_{bp} at

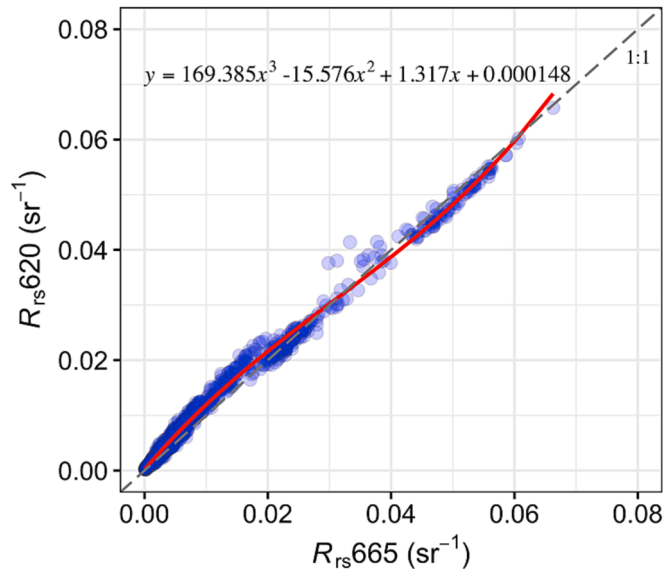


Fig. 3. Polynomial fit of the *in situ* reflectance data ($N = 1265$) for estimating $R_{rs}(620)$ from $R_{rs}(665)$.

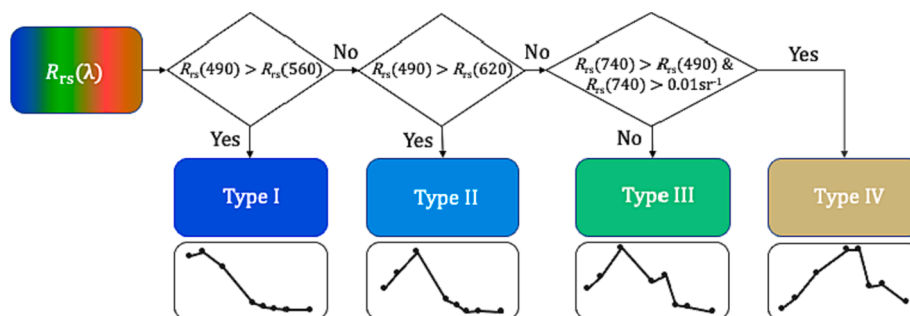


Fig. 2. Flow chart of water type classification for TSS estimation. An example spectral shape is displayed for each water type, where black dots represent the Sentinel-2 MSI bands.

Table 2Median $1/b_{bp}^*$ values at MSI bands convolved from Synthetic Dataset I.

Band (nm)	$1/b_{bp}^*$ (g/m ²)	Band (nm)	$1/b_{bp}^*$ (g/m ²)
443	61.875	705	124.771
490	75.352	740	134.918
560	94.488	783	143.643
665	113.875	865	166.074

the reference band (λ_0) according to water types (Eqs. (2)–(10)); and (4) estimate TSS using Eq. 1, where b_{bp}^* is taken from Table 2. The source code of the proposed TSS estimation method is available via <https://github.com/DalinJiang/TSS>.

3.3. Accuracy assessment

We used the root mean square error (RMSE), the median absolute percentage error (MAPE), Bias, and the slope of regression analysis (in log scale) to evaluate the TSS estimation results. The use of log scale is because of the log distribution of TSS data in this study (Fig. 1a).

$$\text{RMSE} = \sqrt{\frac{\sum_{i=1}^N [\log_{10}(X_{\text{estimated},i}) - \log_{10}(X_{\text{measured},i})]^2}{N}} \quad (12)$$

$$\text{MAPE} = \text{median}\left(\left|\frac{X_{\text{estimated},i} - X_{\text{measured},i}}{X_{\text{measured},i}}\right| \cdot 100\%\right) \quad (13)$$

$$\text{Bias} = 10^Y - 1, Y = \frac{\sum_{i=1}^N [\log_{10}(X_{\text{estimated},i}) - \log_{10}(X_{\text{measured},i})]}{N} \quad (14)$$

where, X_{measured} is the *in situ* or simulated TSS, $X_{\text{estimated}}$ is the corresponding estimated TSS, and N is the number of data points.

We compared our proposed TSS estimation method with three recently published methods: the semi-analytical algorithm from Nechad et al. (2010), the SOLID method from Balasubramanian et al. (2020), and the MDN method from Pahlevan et al. (2022). The semi-analytical algorithm from Nechad et al. (2010) was developed for turbid waters. This algorithm uses a single band (changeable from visible to NIR bands) for TSS estimation and can be applied to different sensors. We convolved the model coefficients (A^p , B^p and C^p) to MSI bands using MSI spectral response functions based on the hyperspectral values provided in that publication, and then tested the performance of using 665 nm, 704 nm, 740 nm, 783 nm and 865 nm for TSS estimation. Finally, we used 740 nm-estimated TSS for comparison in this study as this band showed the best performance. SOLID is a method for estimating TSS based on b_{bp} , where b_{bp} is estimated from a semi-analytical algorithm (QAA), machine-learning and empirical models according to water type classification (Balasubramanian et al., 2020). MDN is a machine-learning method, which is trained using a large number of *in situ* data collected from global inland and coastal waters, and can retrieve Chl-a, TSS and coloured dissolved organic matter (CDOM) simultaneously (Pahlevan et al., 2022). For SOLID and MDN methods, we directly used the code provided in these publications without any re-calibrating or re-training.

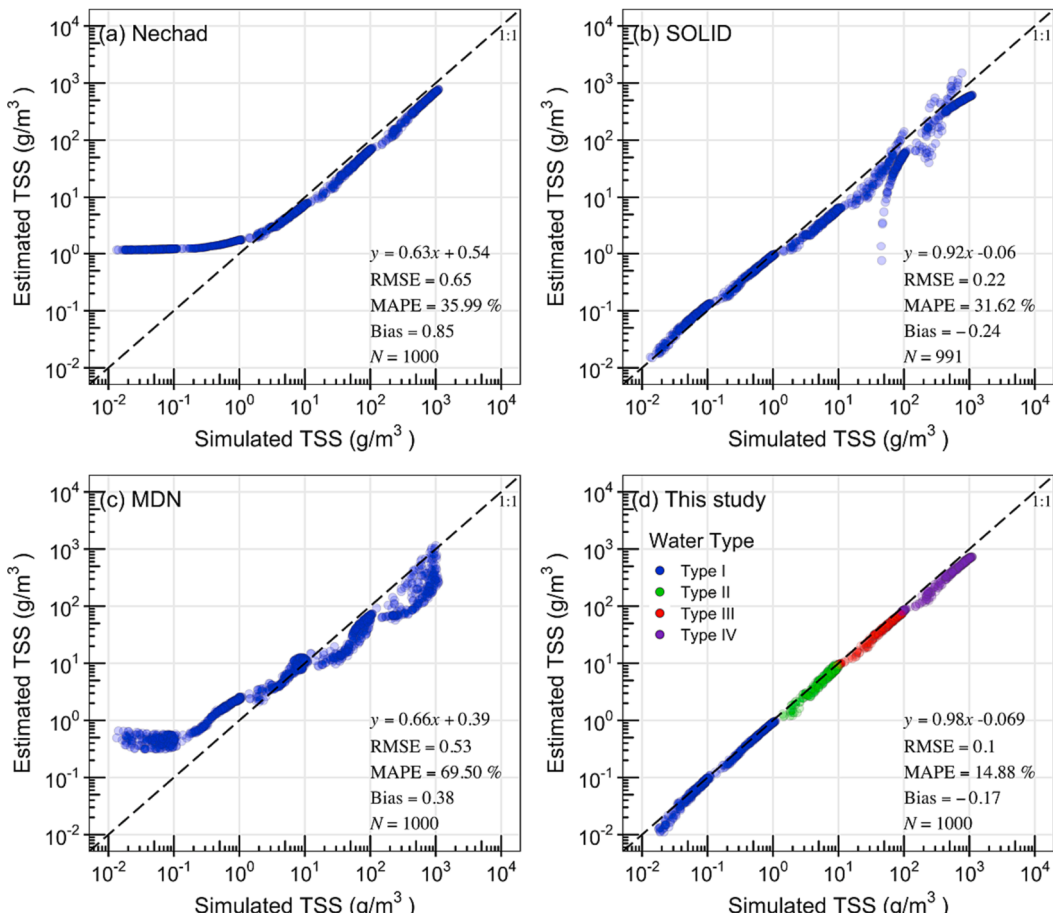


Fig. 4. Validation of the proposed TSS estimation method and comparison with methods from (a) Nechad et al. (2010), (b) SOLID, (c) MDN by using Synthetic Dataset II.

4. Results

4.1. Evaluation of TSS estimation methods using synthetic data

Results using Synthetic Dataset II demonstrate that our proposed method can accurately estimate TSS concentration in clear to extremely turbid waters (Fig. 4d) with a MAPE of 14.88 %. The algorithm slightly underestimated TSS concentration in extremely turbid waters (water type IV) and extremely clear waters ($\text{TSS} < \sim 0.03 \text{ g/m}^3$) with an overall bias of -0.17 . The water type classification sharply separated the four water types showing each in a different TSS range, approximately: clear waters ($< 1 \text{ g/m}^3$), moderately turbid waters ($1\text{--}10 \text{ g/m}^3$), highly turbid waters ($10\text{--}100 \text{ g/m}^3$), and extremely turbid waters ($> 100 \text{ g/m}^3$). Results from the use of Nechad et al. (2010) show good estimates in turbid waters when $\text{TSS} > 2 \text{ g/m}^3$ but overestimations in clear waters when $\text{TSS} < 2 \text{ g/m}^3$ (Fig. 4a). SOLID obtained good estimates in most of the waters but some uncertainties were observed in highly and extremely turbid waters, and nine negative estimates were also found in the results (Fig. 4b). Results from MDN show some overestimations in clear waters and underestimations in turbid waters (Fig. 4c).

4.2. Evaluation of TSS estimation methods using in situ data

For the *in situ* Dataset, the proposed method performs well for all four water types (Fig. 5d), with a MAPE of 31.50 %, and no apparent over- or underestimations (Bias = 0.02). The *in situ* data were not as evenly distributed among the four water types as the data in Synthetic Dataset II (Fig. 4d), with more than half of the data (59 %) classified into water type III, 24 % and 10 % classified into water types II and IV, and only 7 % belonging to water type I. The classification of the *in situ* data into water

types did not separate them as clearly as for Synthetic Dataset II. In particular, water types II and III have some overlaps. Similar to the results using Synthetic Dataset II, the estimated TSS using the methods from Nechad et al. (2010) and MDN show overestimations in clear waters when *in situ* TSS $< 2 \text{ g/m}^3$ (Fig. 5a, 5c). The estimated TSS using SOLID shows some uncertainties in highly and extremely turbid waters, and 24 negative estimates were obtained (Fig. 5b). It should be noted that about half of the *in situ* data in this study were used in MDN training.

4.3. Evaluation of TSS estimation methods using satellite matchups

Using the 40 matchups collected within one hour of MSI overpasses, our proposed method shows an overall good estimation (Fig. 6d). Although the MAPE (41.69 %) is higher than the results from MDN (26.92 %), it shows a better slope and RMSE than all other three methods. The estimated TSS using our proposed method align with the 1:1 line in the graph, while Nechad et al. (2010) and MDN generated overestimations in clear waters (Fig. 6a, 6c), and SOLID generated underestimations in turbid waters and three negative estimates (Fig. 6b). Those are generally the same phenomena as found using Synthetic Dataset II (Fig. 4) and the *in situ* Dataset (Fig. 5). For our proposed method, some largely scattered values were also observed for the estimated TSS in the Plum Island Estuary (blue points in Fig. 6d), and some underestimated TSS for the data from Lake Hibara. These inaccuracies of estimated TSS are possibly caused by the atmospheric correction for MSI images, which resulted in different spectral shapes and/or magnitudes compared to the *in situ* spectra (see discussion for more details).

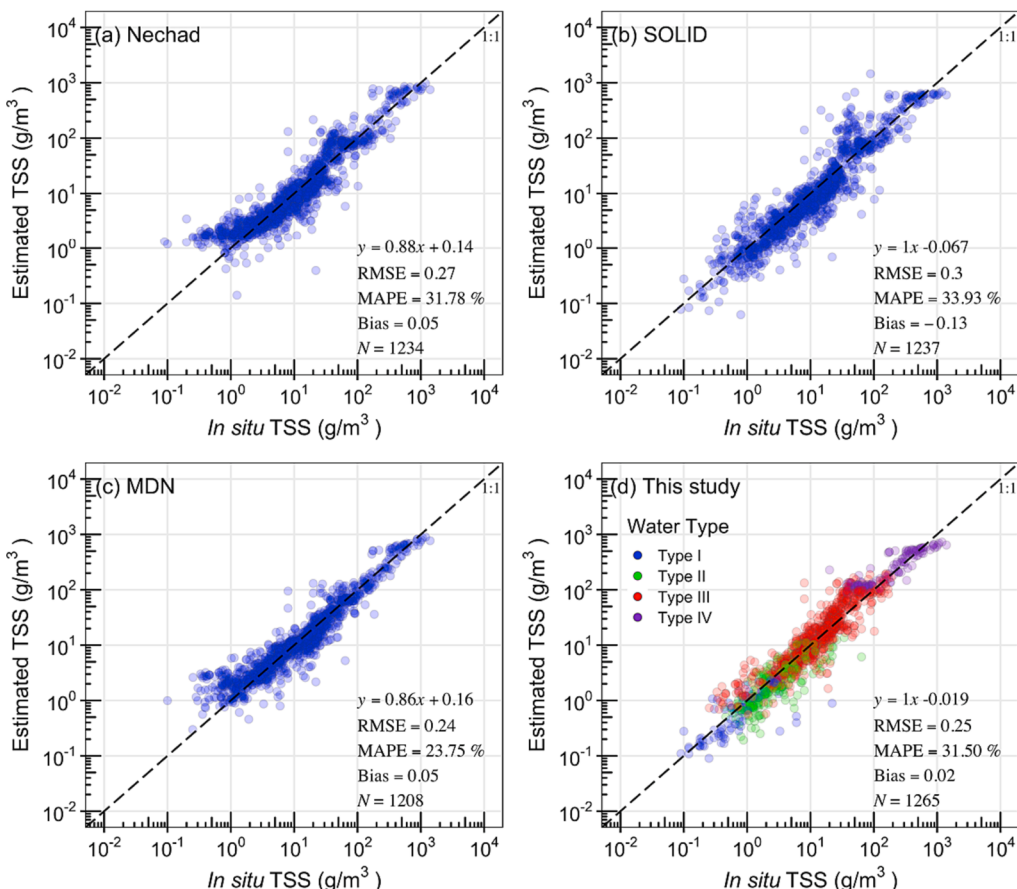


Fig. 5. Validation of the proposed TSS estimation method and comparison with methods from (a) Nechad et al. (2010), (b) SOLID, (c) MDN by using the *in situ* Dataset.

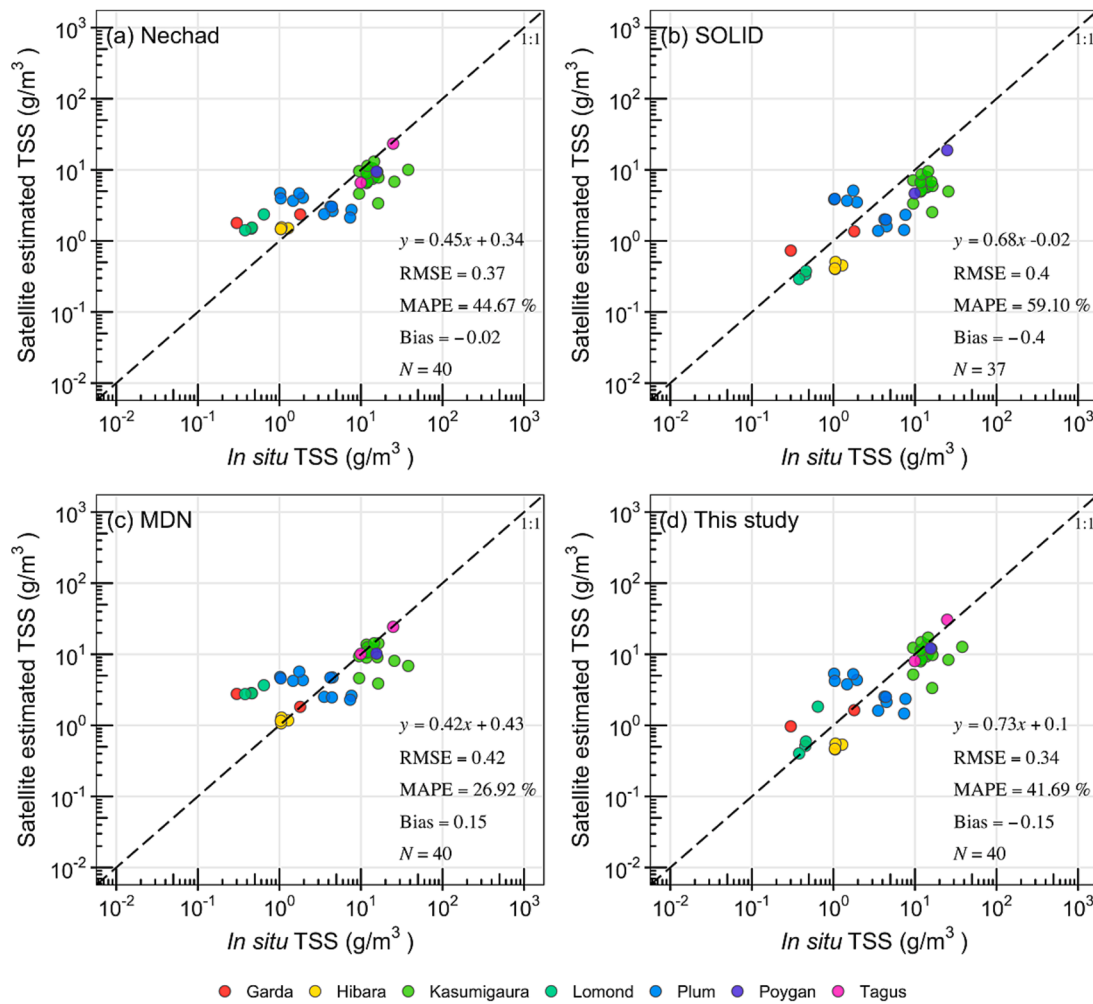


Fig. 6. Validation of the proposed TSS estimation method and comparison with methods from (a) Nechad et al. (2010), (b) SOLID, (c) MDN by using the MSI satellite matchups.

4.4. Advantages of MSI for monitoring TSS in inland and coastal waters

4.4.1. Coastal waters

Application of the proposed TSS method to OLCI and MSI images from 19 October 2021 in the Tagus Estuary (Portugal) shows very similar spatial distributions of TSS, i.e., high TSS in the north because of the Tagus River inflow, medium TSS in the centre, and low TSS in the south because of the ocean connection (Fig. 7c, 7d). TSS values retrieved from OLCI and MSI agree with each other across most of the estuary, but TSS values obtained from OLCI are higher than those obtained from MSI in coastal areas (in the east of the estuary). Possible causes are the overpass difference of ~50 min between OLCI and MSI, the lower tide when OLCI overpassed the estuary, which may have led to more sediment resuspension or bottom reflection. Another reason may be the spatial resolution difference between OLCI and MSI (see discussion for more details).

Compared with OLCI, MSI provides more details of TSS spatial variations. For example, TSS is very high in the Tagus River channel, and decreases when reaching the river mouth. This TSS gradient is clearly shown in the MSI-based map (Fig. 7d), but less clearly displayed in the OLCI-based one (Fig. 7c). Another interesting example is the influence of the bridge in the Tagus Estuary, indicated as a blue arrow in Fig. 7e and 7f. The bridge can clearly be seen on the MSI image, but it does not appear on the OLCI one.

Examining Fig. 7f, we can observe that the spatial pattern of TSS in the MSI image reveals clear strips after the bridge, particularly in the

south-eastern part of the estuary as indicated by the black circle. These TSS strips are caused by the sediment resuspension generated by tidal currents in the piers supporting the bridge, as shown in Fig. 7g. However, this influence on the TSS pattern is not observable in the OLCI image (Fig. 7e).

Station 1 (St.1) to Station 5 (St.5) (white points in Fig. 7e, 7f) represent *in situ* sampling locations visited on the day of satellite overpass in the Tagus Estuary. Fig. 8 shows the transect of TSS across the five *in situ* sampling stations in the Tagus Estuary (white lines in Fig. 7e, 7f). Several interesting observations can be made. Firstly, TSS retrievals from MSI generally agreed with those from OLCI, i.e., TSS is higher close to shore and lower in offshore waters, while some disagreements between the data from the two sensors were observed at both ends of the transect (close to St.1 and St.5). Secondly, the transect of TSS from the MSI image reveals larger and more subtle variations offering detailed information about TSS across the estuary. For instance, the TSS levels between Station 3 (St.3) and Station 4 (St.4) as highlighted by the black box in Fig. 8, correspond to the influence by the bridge as marked by the black circle in Fig. 7f. Thirdly, the TSS values retrieved from OLCI and MSI are very close to *in situ* TSS at St.3 and St.4, but biases were observed for the other three stations. This could be because *in situ* TSS at St.3 and St.4 were collected at a time closer to the satellite overpass (<2h) than at the other stations. Lastly, *in situ* TSS values are generally closer to MSI-derived TSS than OLCI-derived TSS for all five stations.

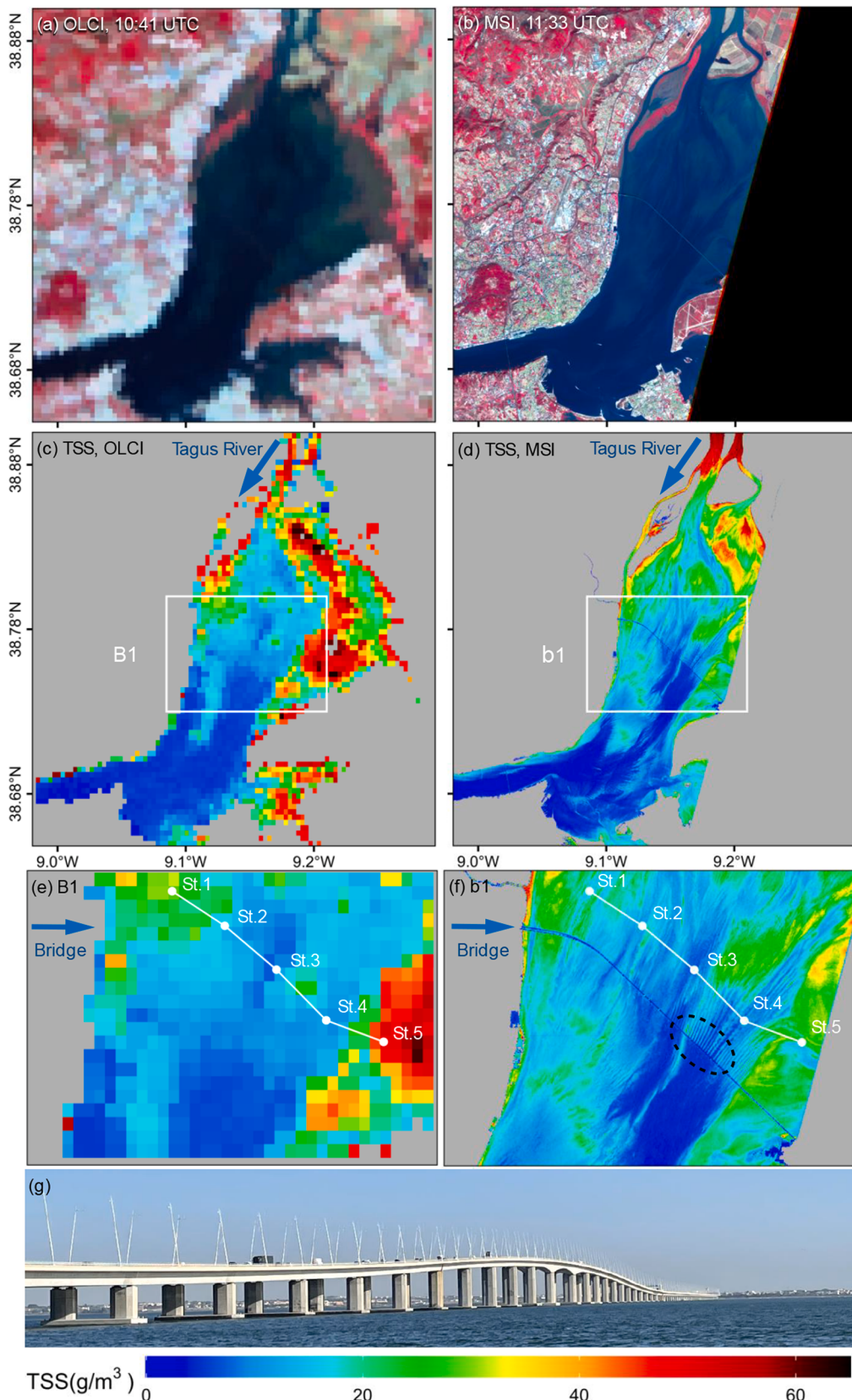


Fig. 7. TSS spatial distribution in the Tagus Estuary on 19 October 2021. (a) OLCI false colour image acquired at 10:41 UTC on 19 October 2021. (b) MSI false colour image acquired at 11:33 UTC on 19 October 2021. (c) TSS estimated from OLCI. (d) TSS estimated from MSI. (e)–(f) TSS maps of subareas of B1 and b1, where white dots are *in situ* sampling stations visited on the day of satellite overpass. (g) Photo of the Vasco da Gama bridge over the Tagus Estuary taken on 19 October 2021 during the CERTO (Copernicus Evolution: Research for harmonised Transitional water Observation) campaign.

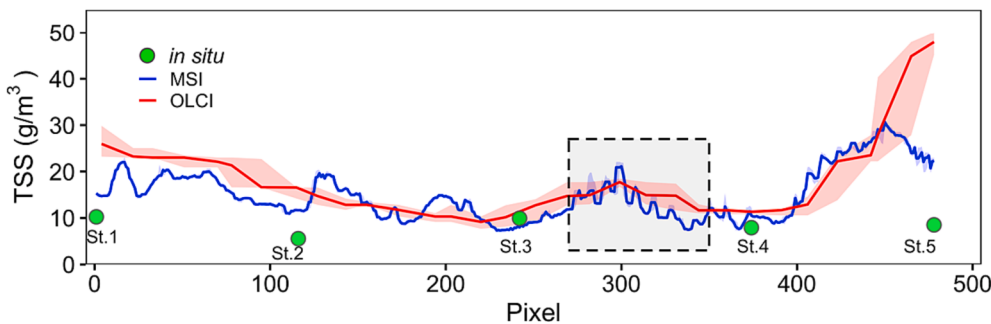


Fig. 8. TSS transect across the Tagus Estuary from St.1 to St.5 in Fig. 7e and 7f. Red line is the TSS transect from OLCI, blue line is the TSS transect from MSI, green dots are *in situ* collected TSS from the day of the satellite overpass. Red shaded area along red line and blue shaded area along blue line indicate the range of TSS within 3×3 pixels.

4.4.2. Inland waters

Fig. 9 shows the TSS maps from OLCI and MSI on 2 February 2020 in Lake Kasumigaura, Japan, just after a heavy precipitation event (35 mm/day and maximum wind speed of 6.1 m/s on 28–29 January 2020). Although the time difference between OLCI and MSI overpasses is ~ 50 min, they show similar TSS values and spatial distributions with low TSS in the northeast and centre of the lake, and high TSS in the north, west and south of the lake (Fig. 9c, d). Compared to OLCI, MSI provides a more detailed spatial distribution of TSS. For example, the TSS eddies in the centre of the lake (Fig. 9d) and the south-eastern lake (Fig. 9j) were clearly observed from MSI but not through OLCI.

One of the most important advantages of MSI over OLCI is the provision of a detailed TSS distribution map for nearshore waters (e.g., river mouths), which are more influenced by the proximity to land compared to the lake centre, and are essential habitats for aquatic macrophytes and animals. A1, A2 and A3 in Fig. 9c (OLCI) cover the same area as a1, a2 and a3 in Fig. 9d (MSI), and are adjacent to three river mouths (Sakura River, Koise River and Shintone River) in Lake Kasumigaura. Due to the heavy precipitation three days before the satellite overpass, a stream of particles entered the lake from rivers together with sediment resuspension in shallow river mouths. TSS in the vicinity of the river mouths is expectedly higher than in other parts of the lake. In the Sakura River mouth, the change of TSS from the river channel to the lake is clearly shown in the MSI-based map (Fig. 9h), but this change in TSS cannot be observed in the OLCI-based map (Fig. 9e). In the Koise River mouth, TSS distribution can be hardly seen from OLCI (Fig. 9f) because of the small water area, but its variations can be clearly observed from MSI (Fig. 9i). By examining Fig. 9j, we can clearly see the extremely high TSS in the Shintone River mouth in the MSI image, as well as the river plume (and/or sediment resuspension) along the south coast of the lake. However, these features are not observable using OLCI, as shown in Fig. 9g.

4.5. Algorithm application for long-term TSS monitoring in Lake Kasumigaura

Fig. 10 shows the long-term TSS from *in situ* data (blue points), and those estimated from OLCI (green points) and MSI images (red points) at the seven stations in Lake Kasumigaura (Fig. 1b). For each site, TSS observations from both satellite sensors are more frequent than *in situ* data. The number of valid TSS observations from OLCI is greater than that from MSI. Taking site 9 between 2017 and 2020 as an example, there were 302 TSS values from OLCI, 119 from MSI, and 36 from *in situ* measurements.

Both MSI-derived and OLCI-derived TSS time-series agree well with the *in situ* time-series, with higher TSS in summer and lower TSS in winter. Fig. 11 shows the comparison of validations using MSI and OLCI matchups, where matchups are *in situ* data collected on the same day of satellite overpass. Both MSI-derived and OLCI-derived TSS show good agreement with *in situ* TSS with a MAPE of 18.78 % and 26.70 %,

respectively. It is also found that OLCI-derived TSS are overall slightly higher than MSI-derived TSS, and MSI-derived TSS are closer to *in situ* TSS with a slightly lower MAPE by comparing the estimated TSS at the same station on the same date (blue points in Fig. 11).

Fig. 10 also shows some events with extremely high TSS in the studied period in Lake Kasumigaura. By using the meteorological data, we found that these high TSS events coincided with typhoons passing over the lake (grey shaded areas in Fig. 12). When typhoons passed over Lake Kasumigaura, the precipitation, wind speed and TSS increased concurrently. This phenomenon was more pronounced in 2019 compared to other years. This is probably associated with increased sediment flux from rivers to the lake due to increased precipitation, and/or the stronger sediment resuspension at higher wind speeds because the lake is very shallow, as shown in the example in Fig. 9.

5. Discussion

5.1. Applicability of the TSS estimation method

Based on the framework developed by Jiang et al. (2021), we proposed a semi-analytical method to estimate TSS from Sentinel-2 MSI. Our method involved creating a model for estimating $R_{rs}(620)$, a band originally unavailable on MSI, and recalibrating the coefficient of b^*_{bp} . Validations using synthetic data (Fig. 4), *in situ* data (Fig. 5), and satellite matchups (Fig. 6) showed that this method can provide accurate TSS estimates for waters across a wide range of turbidity levels.

The use of $R_{rs}(620)$ for water type classification is necessary. We tested the use of $R_{rs}(665)$ instead of $R_{rs}(620)$ for water type classification, but misclassifications of water type and clear underestimations of TSS were found for waters at the boundary between water types II and III for synthetic and *in situ* data. We empirically constructed a model for estimating $R_{rs}(620)$ based on *in situ* spectra, where although a good non-linear relationship between $R_{rs}(620)$ and $R_{rs}(665)$ was obtained (Fig. 3), some uncertainties in the estimated $R_{rs}(620)$ are inevitable. However, the estimated $R_{rs}(620)$ is only used to distinguish water types II and III (Fig. 2), and is not used in TSS estimation. Therefore, its accuracy only influences the distinction of those waters which are close to the boundary between water types II and III. As such waters share similar turbidity levels, misclassification of water type due to errors in estimated $R_{rs}(620)$ is not likely to significantly influence TSS estimation. For example, when we added ± 15 % errors to the estimated $R_{rs}(620)$ in Synthetic Dataset II, the results of estimated TSS showed very similar accuracy ($RMSE = 0.11$) to the results in Fig. 4d ($RMSE = 0.10$). In addition, for those waters which are close to the boundary between water types II and III, estimating TSS using either 665 nm or 740 nm will provide similar results. For example, for the data for which the difference between $R_{rs}(490)$ and $R_{rs}(620)$ was less than $\sim 0.002 \text{ sr}^{-1}$ in Synthetic Dataset II ($N = 152$), the difference between TSS estimated using 665 nm and 740 nm was 5.7 %.

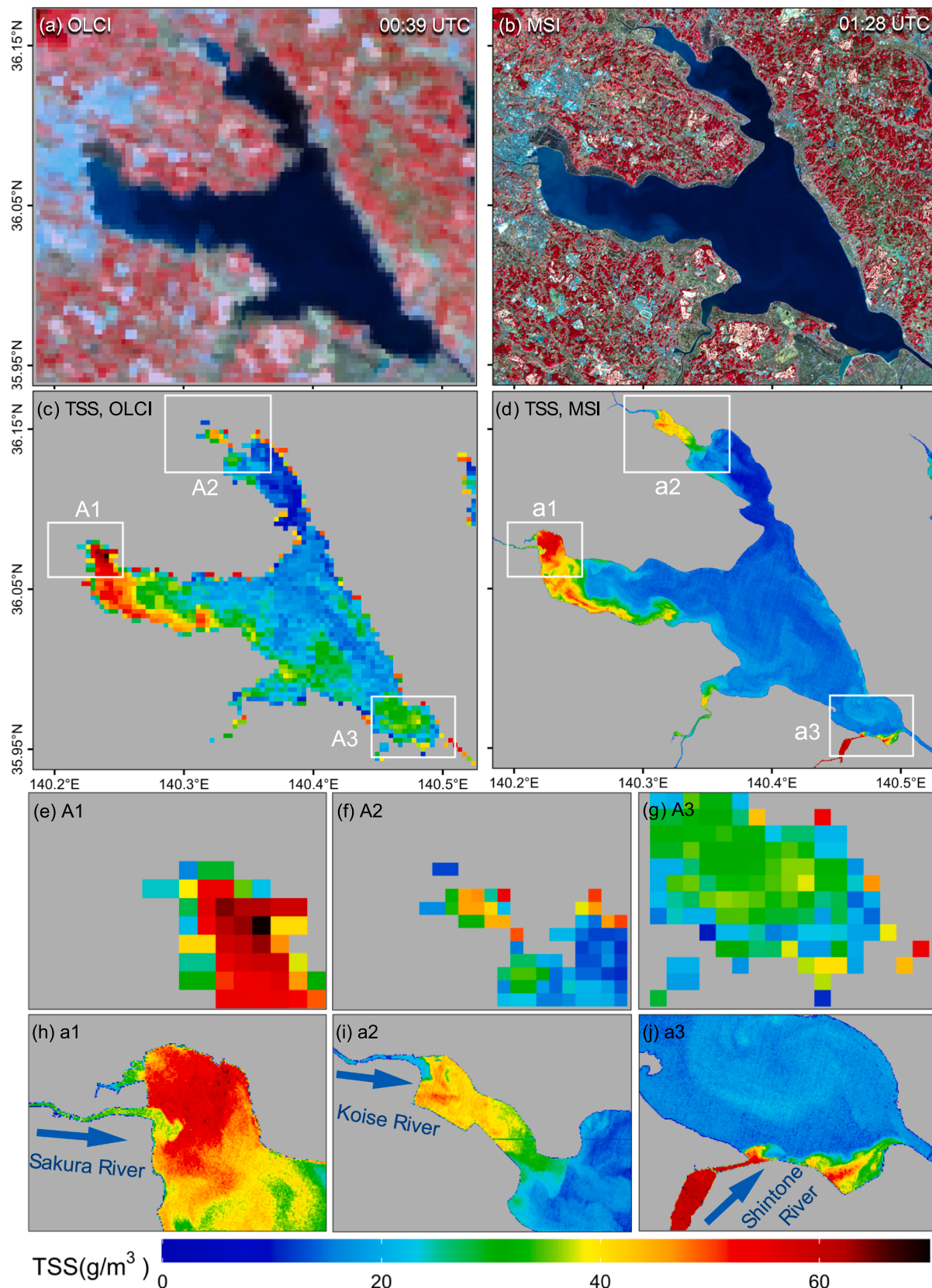


Fig. 9. TSS spatial distribution across Lake Kasumigaura on 2 February 2020, just after a heavy precipitation event on 28–29 January 2020. (a) OLCI false colour image acquired at 00:39 UTC on 2 February 2020. (b) MSI false colour image acquired at 01:28 UTC on 2 February 2020. (c) TSS map from OLCI. (d) TSS map from MSI. (e)–(g) TSS in the Sakura, Koise and Shintone River mouths from OLCI. (h)–(j) TSS in the Sakura, Koise and Shintone River mouths from MSI.

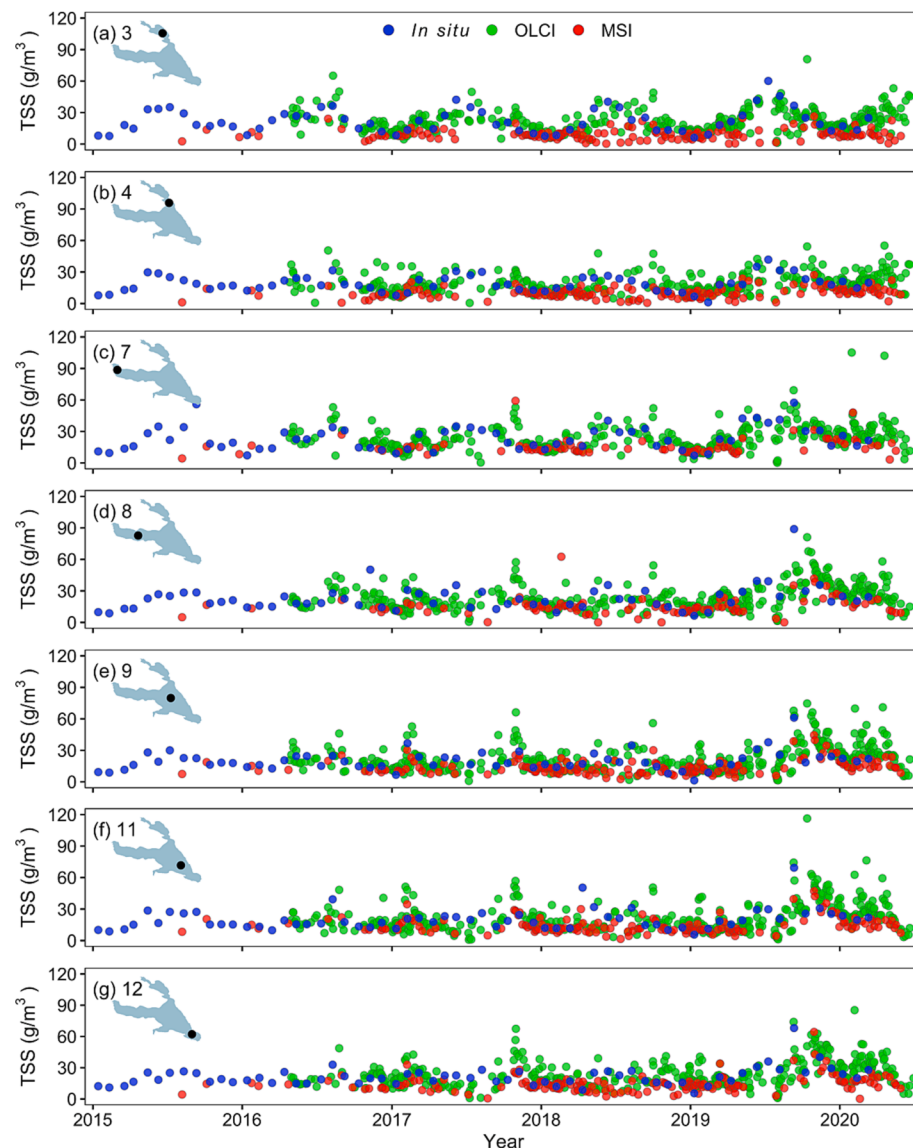


Fig. 10. Long-term TSS during 2015–2020 for Lake Kasumigaura in Japan. Blue dots are *in situ* TSS, green dots are estimated TSS from OLCI images, red dots are estimated TSS from MSI images. Black dots on the map are the locations of monitoring stations in Lake Kasumigaura as in Fig. 1b.

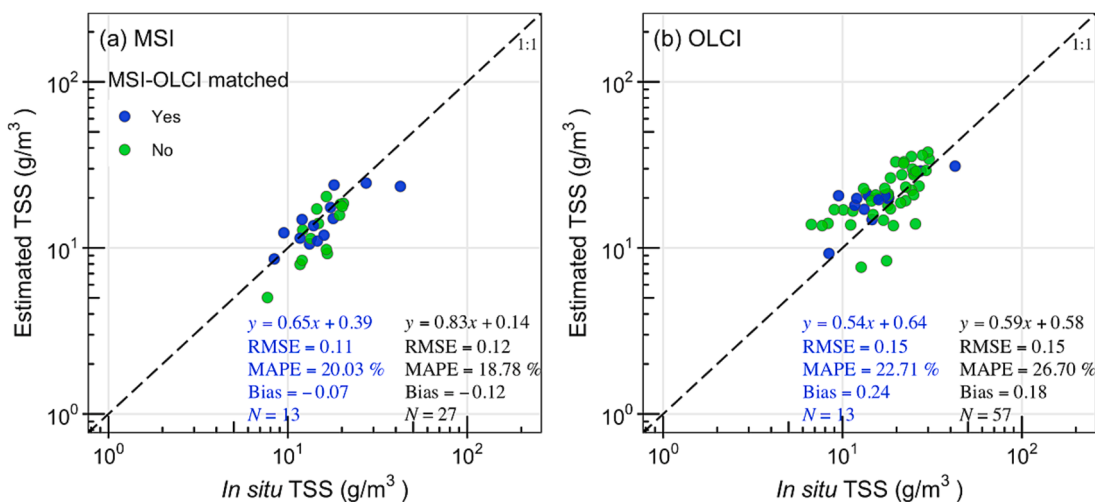


Fig. 11. Comparison of validations using matchups from (a) MSI and (b) OLCI in Lake Kasumigaura, where matchups are *in situ* data collected on the same day of MSI or OLCI overpasses. Blue dots represent matchups that are from the same station and the same day for MSI and OLCI (where ‘MSI-OLCI matched’ shows ‘yes’, $N = 13$).

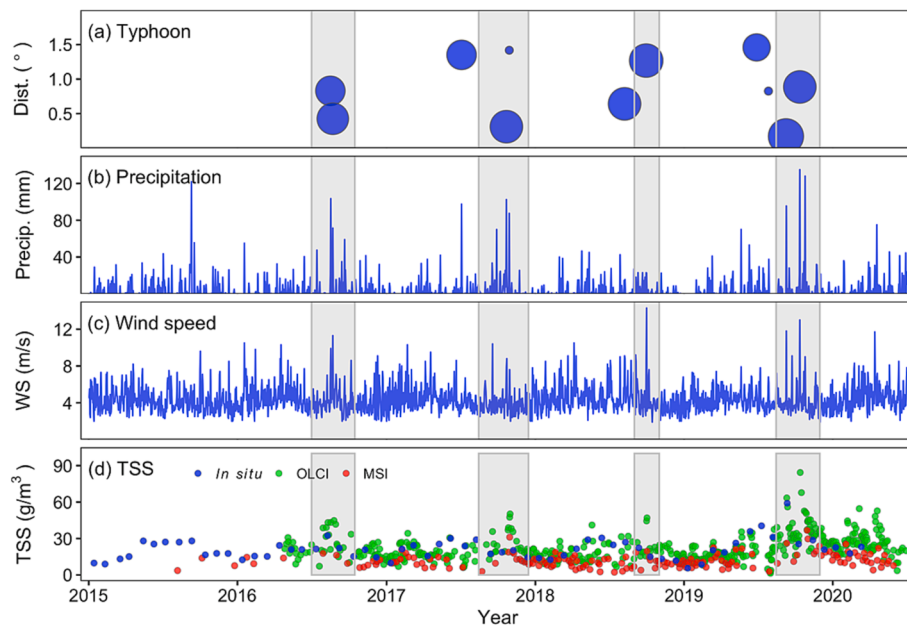


Fig. 12. (a) Typhoons passing over Lake Kasumigaura, where the size of the blue dots indicates the relative magnitude of the typhoon, and the y-axis indicates the distance between typhoon and lake centre while passing. (b)–(c) Precipitation and maximum wind speed at Tsuchiura meteorological station, which is at the nearshore of Lake Kasumigaura. (d) Average *in situ*, OLCI estimated and MSI-estimated TSS at the seven monitoring stations in Lake Kasumigaura.

To test the uncertainty of TSS estimation at water type boundaries, we compared TSS estimated from R_{rs} at two different reference bands corresponding to two neighbouring water types (e.g., 560 nm and 665 nm for water types I and II). Highly consistent TSS estimates at all three water type boundaries indicate that the proposed method can estimate TSS seamlessly between different water types (Fig. 13). However, we

observed an inconsistency of TSS estimates between using 665 nm and 740 nm as reference bands for waters at the boundary between water types II and III when $|R_{rs}(490) - R_{rs}(620)| > 0.002 \text{ sr}^{-1}$ (Fig. 13b, e). That means inaccurate atmospheric correction or $R_{rs}(620)$ estimation may lead to misclassification of water type, and finally cause uncertainties of TSS estimation, but only when the error of the relative

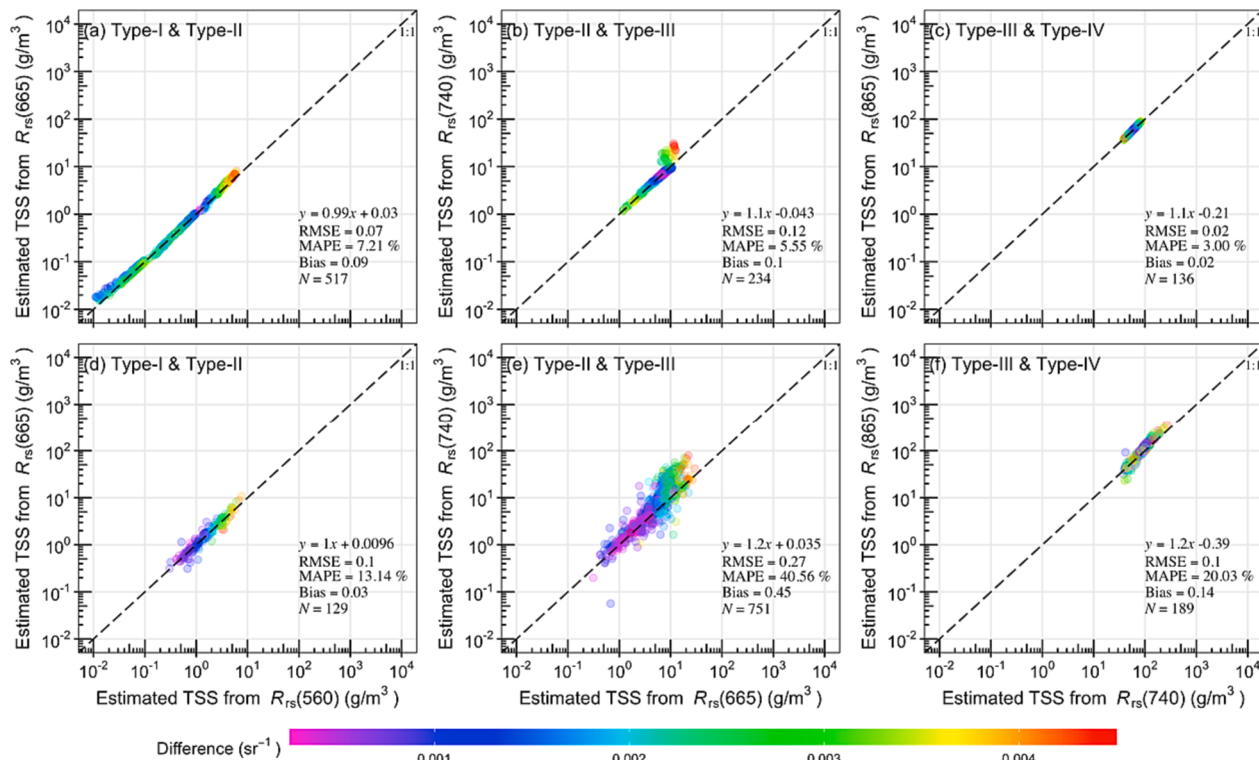


Fig. 13. Comparison of estimated TSS between using two reference bands corresponding to two neighbouring water types for waters at water type boundaries. A water type boundary was defined as having an absolute R_{rs} difference between the two wave bands used for water type classification smaller than 0.005 sr^{-1} . (a)–(c) are results from Synthetic Dataset II, (d)–(f) are results from *in situ* Dataset. Colour indicates the R_{rs} difference between the two wave bands used for water type classification.

difference between $R_{rs}(490)$ and $R_{rs}(620)$ is higher than $\sim 0.002 \text{ sr}^{-1}$.

The b^*_{bp} values were re-calibrated to optimise them for MSI (Table 2), although we didn't find significant improvements in TSS estimation for the data used in this study by using the re-calibrated b^*_{bp} rather than the b^*_{bp} for MERIS and OLCI in Jiang et al. (2021). It was nonetheless necessary to do, because the difference of bandwidths and band centres between MSI and the other sensors (e.g., the large difference of the 740 nm band for MSI and 754 nm band for OLCI (MERIS) used in the TSS estimation for water type III) may lead to errors in TSS estimation (Cao et al., 2019; Ford & Vodacek, 2020). Following the same approach as in Jiang et al. (2021), we used the median b^*_{bp} values from simulations for TSS estimation from MSI. There might have been some instances where b^*_{bp} are different from our simulated values or b_{bp} doesn't follow a power function (Binding et al., 2019; Xu et al., 2021), such as the one we adopted in our simulations, and users are encouraged to replace the median b^*_{bp} with more realistic or *in situ* measured values where available to improve the TSS estimation accuracy.

The semi-analytical method proposed in this study improved TSS estimation compared to the other existing methods (Figs. 4, 5, 6), with more accurate estimates in clear waters compared to the semi-analytical method from Nechad et al. (2010) and MDN as well as more accurate and valid estimates compared to SOLID. These improvements make the proposed method applicable from clear to extremely turbid waters with less uncertainties and benefit the water quality monitoring of inland and coastal waters as these waters cover a wide range of turbidity levels. The proposed method can also increase the confidence when estimating TSS for a water body without prior knowledge of turbidity levels. Some underestimations, especially for extremely turbid waters, were observed for the proposed method (Fig. 4d), because a might be higher than a_w due to high turbidity, but we assumed $a \approx a_w$. Further studies are needed to address this problem. It should also be emphasised that the accuracy of the proposed method will highly depend on the accuracy of the R_{rs} magnitude of the reference band used for TSS estimation (Jiang et al., 2020; Jiang et al., 2021). Our test using seven MSI matchups in Lake Kasumigaura revealed that the error of estimated TSS has a very high correlation with the error of R_{rs} with an R^2 of 0.94 (Fig. 14). This necessitates an accurate measurement of *in situ* R_{rs} or atmospheric correction of the satellite images when using our proposed method.

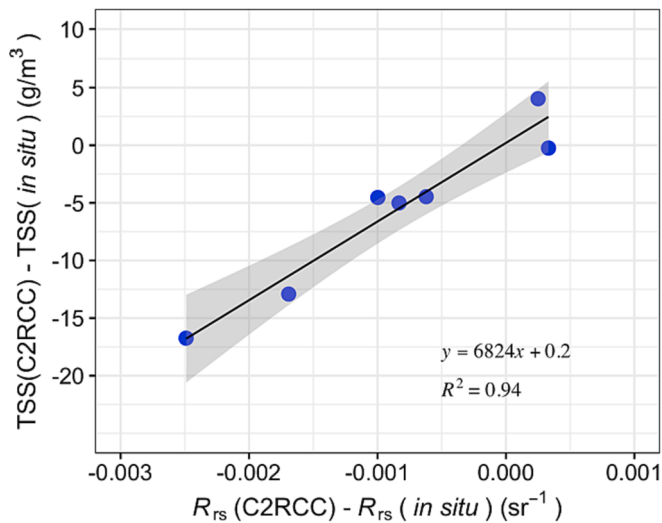


Fig. 14. Relationship between R_{rs} error and estimated TSS error for seven MSI matchups obtained on 27 October and 29 November 2016 in Lake Kasumigaura, Japan. X-axis is the difference between C2RCC-derived R_{rs} and *in situ* R_{rs} , Y-axis is the difference between estimated TSS using C2RCC-derived R_{rs} and *in situ* TSS.

5.2. Advantages of MSI in TSS monitoring

MSI has clear advantages in TSS monitoring over ocean colour sensors (e.g., MERIS and OLCI), because of its high spatial resolution, which can make small water bodies observable and provide more details of TSS spatial distributions. The use of MSI and the method proposed in this study can expand TSS monitoring to water bodies with a minimum observable area of $\sim 0.0036 \text{ km}^2$ ($0.02 \text{ km} \times 0.02 \text{ km} \times 9 = 0.0036 \text{ km}^2$) accounting for $20 \text{ m} \times 20 \text{ m}$ spatial resolution and at least 9 pixels for a water body). This will make at least $\sim 2.3 \times 10^7$ more lakes, i.e., $\sim 20\%$ of the global lakes with an area between 0.01 and 0.1 km^2 (Verpoorter et al., 2014) observable compared to using OLCI images (considering a minimum observable area of more than 0.1 km^2 for OLCI). In addition to small lakes, TSS monitoring with MSI can expand to small bays, estuaries, rivers and lagoons where ocean colour sensors are not applicable, or can provide more details of TSS spatial variations where such sensors cannot. The examples in Figs. 7 and 9 in this study clearly show the advantage of TSS mapping using MSI for rivers, river mouths, and nearshore waters and detecting those detailed spatial variations near bridges, which are not observable in OLCI images. It is well known that the above-mentioned inland and coastal waters are closely linked to human activities (Kummu et al., 2011; Small & Nicholls, 2003) and TSS observations from MSI can provide valuable supporting information for environmental management and decision-making for those water bodies.

We found that the MSI image-derived TSS are closer to *in situ* TSS when compared to OLCI image-derived TSS although both of them agree well with *in situ* TSS (Figs. 8, 11). For Synthetic Dataset II and *in situ* spectra, we also found the estimated TSS using MSI bands showed higher accuracies than the ones using OLCI bands for water types I and II. The reasons why MSI-derived TSS are closer to *in situ* TSS than OLCI-derived TSS may include: (1) the spectral resolution (band width) effect, which influences the sensitivity of sensors in detecting TSS (Cao et al., 2019; Ford & Vodacek, 2020). MSI has wider bands, which will result in higher R_{rs} compared to OLCI when convolving 1 nm spectra to its bands, where the higher R_{rs} will compensate underestimations from the assumption of $a \approx a_w$ in our proposed method, which is more influential for water type II than the other three water types. For example, the average $R_{rs}(665)$ of water type II of the *in situ* Dataset ($N = 301$) is 0.00260 sr^{-1} for MSI, which is higher than that for OLCI (0.00246 sr^{-1}); (2) the spatial resolution effect, which influences the estimated TSS particularly in non-spatially uniform water areas (Dorji & Fearn, 2017; Fisher et al., 2018). MSI has higher spatial resolution, so the average TSS within 3×3 MSI pixels covering a smaller area (0.0036 km^2) is closer to *in situ* TSS than that within 3×3 OLCI pixels covering a wider area (0.81 km^2). Fig. 15 shows an example of estimated TSS in the $900 \text{ m} \times 900 \text{ m}$ area surrounding St.1 in the Tagus Estuary (Fig. 7) and from both the OLCI image (Fig. 15a) and MSI image (Fig. 15b), it can be seen that the MSI-estimated TSS has more spatial variations compared to OLCI-estimated TSS in the same area. Moreover, near St.1 there is a channel with lower TSS (blue pixels in Fig. 15b) than to the northwest and southeast (green to yellow pixels in Fig. 15b). This spatial variation can be observed from MSI but not from OLCI. Therefore, when extracting TSS from a 3×3 -pixel window for validation, the estimated TSS from MSI is closer to *in situ* TSS than that from OLCI for this station (Fig. 8). This confirms that the influence of spatial resolution cannot be ignored as it may lead to uncertainties when using satellite-derived R_{rs} and *in situ* collected TSS as inputs for empirical model calibration or machine learning model training, because they are not corresponding to each other, especially for coarse spatial resolution images.

Although some slight differences were observed between MSI-derived and OLCI-derived TSS, the results in this study showed that these sensors can provide overall consistent TSS time-series (Fig. 10) and TSS spatial distributions on the same overpass dates (Figs. 7, 8, 9). This indicates that OLCI and MSI can be used collaboratively for TSS monitoring in inland and coastal waters, where OLCI can provide high

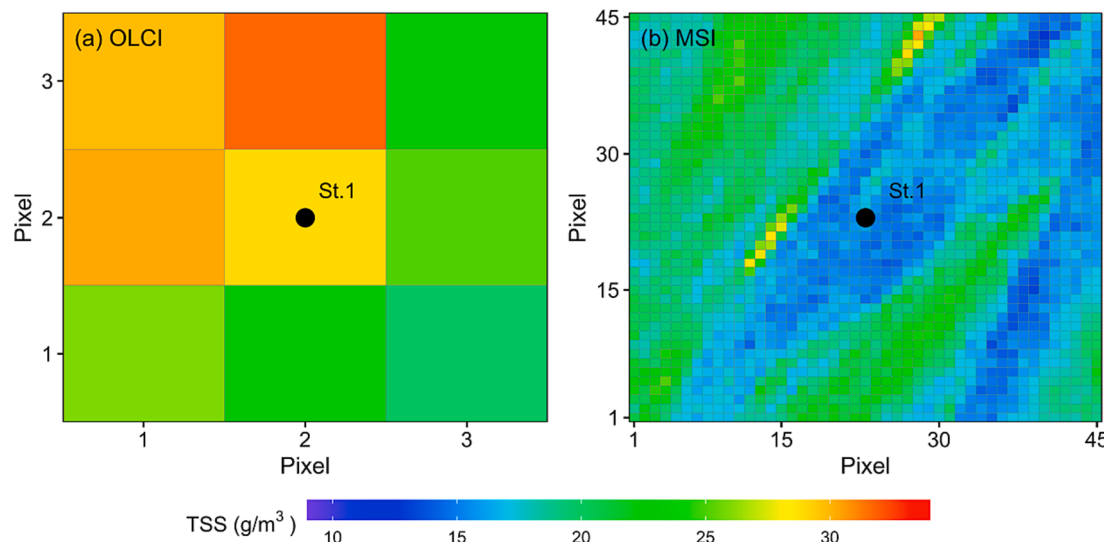


Fig. 15. TSS spatial distribution in an area of $900 \text{ m} \times 900 \text{ m}$ surrounding the *in situ* sampling station St.1 in the Tagus Estuary from OLCI and MSI images on the same day as shown in Fig. 7. (a) $900 \text{ m} \times 900 \text{ m}$ surrounding St.1 from the OLCI image (i.e., 3×3 pixels). (b) $900 \text{ m} \times 900 \text{ m}$ surrounding St.1 from the MSI image (i.e., 45×45 pixels).

monitoring frequency and MSI can provide high spatial resolution, which can enhance the ability of TSS monitoring from satellite images and provide more potential for water pollution or extreme event monitoring. In the example of Lake Kasumigaura, OLCI can monitor high TSS events because of heavy precipitation and/or sediment resuspension (Fig. 12), and MSI can provide more details as to where such high TSS is located (Fig. 9). In addition, as there is a time difference between OLCI and MSI overpasses (e.g., ~ 50 mins in Figs. 7, 9), these two sensors can be used to monitor TSS changes on the same day in highly dynamic waters.

5.3. Atmospheric correction and satellite matchups

This study used the C2RCC atmospheric correction method, which is based on comparisons of four different atmospheric correction methods, namely ACOLITE (Vanhellemont, 2019), C2RCC (Brockmann et al., 2016), Polymer (Steinmetz et al., 2011) and Sen2cor (Main-Knorn et al., 2017). In a comparison of satellite-derived R_{rs} to *in situ* R_{rs} collected within one hour of satellite overpasses from our studied waters, C2RCC and Polymer showed similar accuracy and better performance than the other two methods (Figure S1 in supplementary). Moreover, C2RCC produced more accurate results than Polymer in retrieving TSS time-series in Lake Kasumigaura (Figure S2 in supplementary) because of its higher accuracy in the NIR bands, which were used for estimating TSS in this lake (mainly 740 nm). However, C2RCC still showed some uncertainties in derived R_{rs} . For example, the atmospherically corrected spectra showed reflectance peaks at 490 nm in Lake Hibara, which were then classified as water type I. Contrarily, the reflectance peaks from *in situ* spectra were at 560 nm, which were classified as water type II. This misclassification of water type led to underestimations of TSS (yellow points in Fig. 6d). Some of the spectra from atmospherically corrected MSI images showed similar shapes to *in situ* spectra from the Plum Island Estuary, but their magnitudes were lower than those of the *in situ* spectra, which finally led to underestimations of TSS (blue points below 1:1 line in Fig. 6). Some TSS underestimations observed in sites 3 and 4 in Lake Kasumigaura (Fig. 10) are also possible because of underestimated R_{rs} from C2RCC. Those uncertainties could constrain the application of the proposed TSS method to MSI images in inland and coastal waters. Because of their small size, adjacency to land and optical complexity (Palmer et al., 2015; Jiang et al., 2023), an atmospheric correction method which can accommodate waters with a wide range of

bio-optical properties, different aerosol types and adjacency effects is necessary for inland and coastal water applications. This requires further developments on the atmospheric correction methodology.

Matchups for TSS validation in this study are restricted to within one hour of satellite overpass. This restriction is very important for highly dynamic waters such as estuaries or river mouths, where the bio-optical properties can change within a short period of time due to tides or currents (Eleveld et al., 2014). This is exemplified for the Tagus Estuary shown in Fig. 8, where *in situ* TSS at St.3 and St.4 were collected within ~ 23 min and ~ 66 min difference to the MSI overpass respectively, and agreed with satellite retrievals. However, *in situ* TSS at St.2 and St.5 were collected 3.4 and 2.1 h after the MSI overpass respectively, when water in the estuary had changed considerably because of tides. Thus, they showed large disagreement with satellite retrievals. Some TSS differences were observed between OLCI and MSI in Fig. 7c and d, and these differences may also be due to the quick change in water conditions. Therefore, it is important to consider the time difference between *in situ* data collection and satellite overpass when performing satellite product validations, especially for highly dynamic waters.

6. Conclusions

We proposed a semi-analytical method for estimating TSS from Sentinel-2 MSI images in this study with the aim of providing high spatial resolution TSS for inland and coastal waters. Validation and comparison using a simulated dataset, globally collected *in situ* data and satellite matchups showed that our approach outperformed other existing methods and can be applied from clear to extremely turbid waters resulting in accurate TSS estimation. Results also showed the significant advantages of MSI images in TSS mapping for rivers, river mouths and other nearshore waters. Applying the proposed TSS method for MSI with prior C2RCC atmospheric correction led to reasonable long-term TSS estimates in Lake Kasumigaura, which showed good agreement with *in situ* and OLCI-derived TSS time-series. Although MSI-derived TSS are closer to *in situ* TSS than OLCI-derived TSS, both of them agree well with *in situ* data and can be used collaboratively for TSS monitoring. When it comes to highly dynamic waters, it is essential to restrict the time difference between *in situ* data collection and satellite overpass for validating satellite products.

Declaration of Competing Interest

The authors declare that they have no known competing financial interests or personal relationships that could have appeared to influence the work reported in this paper.

Acknowledgements

This research was supported in part by the European Union's (EU) Horizon 2020 CERTO (Copernicus Evolution: Research for harmonised Transitional water Observation) project (No. 870349), the Fundação para a Ciência e a Tecnologia (FCT) through the Scientific Employment Stimulus Programme (CEECIND/0095/2017), and the Fundação para a Ciência e a Tecnologia through the strategic projects (UID/MAR/04292/2020, LA/P/0069/2020) granted to MARE and ARNET. We thank the European Space Agency (ESA) and USGS for providing the Sentinel-2 MSI and Sentinel-3 OLCI images. We also thank the National Institute for Environmental Studies (NIES), Japan for providing the *in situ* TSS data in Lake Kasumigaura, the Japan Meteorological Agency (JMA) for providing the typhoon and meteorological data, and Claudia Giardino and Mariano Bresciani from the National Research Council of Italy (CNR) for providing the *in situ* data in Lake Garda and Lake Trasimeno. We also acknowledge the editorial team and reviewers for their time and effort, valuable comments and suggestions.

Appendix A. Supplementary material

Supplementary data to this article can be found online at <https://doi.org/10.1016/j.isprsjprs.2023.09.020>.

References

- Balasubramanian, S.V., Pahlevan, N., Smith, B., Binding, C., Schalles, J., Loisel, H., Boss, E., 2020. Robust algorithm for estimating total suspended solids (TSS) in inland and nearshore coastal waters. *Remote Sens. Environ.* 246, 111768.
- Binding, C.E., Greenberg, T.A., Bukata, R.P., 2012. An analysis of MODIS-derived algal and mineral turbidity in Lake Erie. *J. Great Lakes Res.* 38 (1), 107–116.
- Binding, C.E., Zastepa, A., Zeng, C., 2019. The impact of phytoplankton community composition on optical properties and satellite observations of the 2017 western Lake Erie algal bloom. *J. Great Lakes Res.* 45 (3), 573–586.
- Brockmann, C., Doerffer, R., Peters, M., Kerstin, S., Embacher, S., Ruescas, A., 2016. Evolution of the C2RCC neural network for Sentinel 2 and 3 for the retrieval of ocean colour products in normal and extreme optically complex waters. *Living Planet Symposium* 740, 54.
- Brown, R., 1984. Relationships between suspended solids, turbidity, light attenuation, and algal productivity. *Lake Reservoir Manage.* 1 (1), 198–205.
- Cao, Z., Ma, R., Duan, H., Xue, K., 2019. Effects of broad bandwidth on the remote sensing of inland waters: Implications for high spatial resolution satellite data applications. *ISPRS J. Photogramm. Remote Sens.* 153, 110–122.
- Ciancia, E., Campanelli, A., Lacava, T., Palombo, A., Pascucci, S., Pergola, N., Tramutoli, V., 2020. Modeling and multi-temporal characterization of total suspended matter by the combined use of Sentinel 2-MSI and Landsat 8-OLI data: the Pertusillo Lake Case Study (Italy). *Remote Sens. (Basel)* 12 (13), 2147.
- Dorji, P., Fearns, P., 2017. Impact of the spatial resolution of satellite remote sensing sensors in the quantification of total suspended sediment concentration: A case study in turbid waters of Northern Western Australia. *PLoS One* 12 (4), e0175042.
- Drusch, M., Del Bello, U., Carlier, S., Colin, O., Fernandez, V., Gascon, F., Bargellini, P., 2012. Sentinel-2: ESA's optical high-resolution mission for GMES operational services. *Remote Sens. Environ.* 120, 25–36.
- Eleved, M.A., Van der Wal, D., Van Kessel, T., 2014. Estuarine suspended particulate matter concentrations from sun-synchronous satellite remote sensing: Tidal and meteorological effects and biases. *Remote Sens. Environ.* 143, 204–215.
- Fichot, C.G., Downing, B.D., Bergamaschi, B.A., Windham-Myers, L., Marvin-DiPasquale, M., Thompson, D.R., Gierach, M.M., 2016. High-resolution remote sensing of water quality in the San Francisco Bay-Delta Estuary. *Environ. Sci. Technol.* 50 (2), 573–583.
- Fisher, J.R., Acosta, E.A., Dennedy-Frank, P.J., Kroeger, T., Boucher, T.M., 2018. Impact of satellite imagery spatial resolution on land use classification accuracy and modeled water quality. *Remote Sens. Ecol. Conserv.* 4 (2), 137–149.
- Ford, R.T., Vodacek, A., 2020. Determining improvements in Landsat spectral sampling for inland water quality monitoring. *Sci. Remote Sens.* 1, 100005.
- Gons, H.J., Auer, M.T., Effler, S.W., 2008. MERIS satellite chlorophyll mapping of oligotrophic and eutrophic waters in the Laurentian Great Lakes. *Remote Sens. Environ.* 112 (11), 4098–4106.
- Gurlin, D., Gitelson, A.A., Moses, W.J., 2011. Remote estimation of chl-a concentration in turbid productive waters—Return to a simple two-band NIR-red model? *Remote Sens. Environ.* 115 (12), 3479–3490.
- Han, B., Loisel, H., Vantrepotte, V., Mériaux, X., Bryère, P., Ouillon, S., Zhu, J., 2016. Development of a semi-analytical algorithm for the retrieval of suspended particulate matter from remote sensing over clear to very turbid waters. *Remote Sens. (Basel)* 8 (3), 211.
- Heino, J., Alahuhta, J., Bini, L.M., Cai, Y., Heiskanen, A.S., Hellsten, S., Angeler, D.G., 2021. Lakes in the era of global change: Moving beyond single-lake thinking in maintaining biodiversity and ecosystem services. *Biol. Rev.* 96 (1), 89–106.
- IOCCG, 2014. Update of the Quasi-Analytical Algorithm (QAA v6). Available online. http://www.ioccg.org/groups/Software/OCA/QAA_v6_2014209.pdf.
- Jiang, D., Matsushita, B., Setiawan, F., Vundo, A., 2019. An improved algorithm for estimating the Secchi disk depth from remote sensing data based on the new underwater visibility theory. *ISPRS J. Photogramm. Remote Sens.* 152, 13–23.
- Jiang, D., Matsushita, B., Yang, W., 2020. A simple and effective method for removing residual reflected skylight in above-water remote sensing reflectance measurements. *ISPRS J. Photogramm. Remote Sens.* 165, 16–27.
- Jiang, D., Matsushita, B., Pahlevan, N., Gurlin, D., Lehmann, M.K., Fichot, C.G., O'Donnell, D., 2021. Remotely estimating total suspended solids concentration in clear to extremely turbid waters using a novel semi-analytical method. *Remote Sens. Environ.* 258, 112386.
- Jiang, D., Scholze, J., Liu, X., Simis, S.G., Stelzer, K., Müller, D., Spyarakos, E., 2023. A data-driven approach to flag land-affected signals in satellite derived water quality from small lakes. *Int. J. Appl. Earth Obs. Geoinf.* 117, 103188.
- Knaeps, E., Ruddick, K.G., Doxaran, D., Dogliotti, A.I., Nechad, B., Raymaekers, D., Sterckx, S., 2015. A SWIR based algorithm to retrieve total suspended matter in extremely turbid waters. *Remote Sens. Environ.* 168, 66–79.
- Kou, L., Labrie, D., Chylek, P., 1993. Refractive indices of water and ice in the 0.65-to 2.5- μ m spectral range. *Appl. Opt.* 32 (19), 3531–3540.
- Kummü, M., De Moel, H., Ward, P.J., Varis, O., 2011. How close do we live to water? A global analysis of population distance to freshwater bodies. *PLoS One* 6 (6), e20578.
- Lee, Z., Carder, K.L., Arnone, R.A., 2002. Deriving inherent optical properties from water color: a multiband quasi-analytical algorithm for optically deep waters. *Appl. Opt.* 41 (27), 5755–5772.
- Lee, Z. P., Lubac, B., Werde, J., & Arnone, R. 2009. An update of the quasi-analytical algorithm (QAA-v5), open file online at: https://www.ioccg.org/groups/Software/OCA/QAA_v5.pdf.
- Li, P., Ke, Y., Bai, J., Zhang, S., Chen, M., Zhou, D., 2019. Spatiotemporal dynamics of suspended particulate matter in the Yellow River Estuary, China during the past two decades based on time-series Landsat and Sentinel-2 data. *Mar. Pollut. Bull.* 149, 110518.
- Li, H., Li, Q., Shi, T., Hu, S., Wu, G., Zhou, Q., 2017. Application of sentinel 2 MSI images to retrieve suspended particulate matter concentrations in Poyang Lake. *Remote Sens. (Basel)* 9 (7), 761.
- Main-Knorr, M., Pflug, B., Louis, J., Debaecker, V., Müller-Wilm, U., & Gascon, F., (2017). Sen2Cor for sentinel-2. In: *Image and Signal Processing for Remote Sensing XXIII*, vol. 10427, SPIE, pp. 37–48.
- McCullough, G.K., Barber, D., 2007. The effect of suspended solids loading from the Linthipe River on light in Lake Malawi. *J. Great Lakes Res.* 33 (2), 466–482.
- Mobley, C.D., 1999. Estimation of the remote-sensing reflectance from above-surface measurements. *Appl. Opt.* 38 (36), 7442–7455.
- Mueller, J. L., Morel, A., Frouin, R., Davis, C., Arnone, R., Carder, K., Voss, K. (2003). Ocean Optics Protocols for Satellite Ocean Color Sensor Validation, Revision 4. In: Volume III: Radiometric Measurements and Data Analysis Protocols. Goddard Space Flight Space Center, Greenbelt, MD, USA.
- Nechad, B., Ruddick, K.G., Park, Y., 2010. Calibration and validation of a generic multisensor algorithm for mapping of total suspended matter in turbid waters. *Remote Sens. Environ.* 114 (4), 854–866.
- NIES, National Institute for Environmental Studies, 2020. Lake Kasumigaura Database, National Institute for Environmental Studies, Japan. Accessed via. <http://db.cger.nies.go.jp/gem/moni-e/inter/GEMS/database/kasumi/index.html>. on 24-08-2020.
- Novoa, S., Doxaran, D., Ody, A., Vanhelmont, Q., Lafon, V., Lubac, B., Gernez, P., 2017. Atmospheric corrections and multi-conditional algorithm for multi-sensor remote sensing of suspended particulate matter in low-to-high turbidity levels coastal waters. *Remote Sens. (Basel)* 9 (1), 61.
- Oyama, Y., Matsushita, B., Fukushima, T., Matsuhige, K., Imai, A., 2009. Application of spectral decomposition algorithm for mapping water quality in a turbid lake (Lake Kasumigaura, Japan) from Landsat TM data. *ISPRS J. Photogramm. Remote Sens.* 64 (1), 73–85.
- Pahlevan, N., Sarkar, S., Franz, B.A., Balasubramanian, S.V., He, J., 2017. Sentinel-2 MultiSpectral Instrument (MSI) data processing for aquatic science applications: Demonstrations and validations. *Remote Sens. Environ.* 201, 47–56.
- Pahlevan, N., Smith, B., Alikas, K., Anstee, J., Barbosa, C., Binding, C., Ruiz-Verdú, A., 2022. Simultaneous retrieval of selected optical water quality indicators from Landsat-8, Sentinel-2, and Sentinel-3. *Remote Sens. Environ.* 270, 112860.
- Palmer, S.C., Kutser, T., Hunter, P.D., 2015. Remote sensing of inland waters: Challenges, progress and future directions. *Remote Sens. Environ.* 157, 1–8.
- Pope, R.M., Fry, E.S., 1997. Absorption spectrum (380–700 nm) of pure water. II. Integrating cavity measurements. *Appl. Opt.* 36 (33), 8710–8723.
- Quan, X., Fry, E.S., 1995. Empirical equation for the index of refraction of seawater. *Appl. Opt.* 34 (18), 3477–3480.
- Reynaud, A., Lanzanova, D., 2017. A global meta-analysis of the value of ecosystem services provided by lakes. *Ecol. Econ.* 137, 184–194.

- Saberioon, M., Brom, J., Nedbal, V., Souček, P., Císař, P., 2020. Chlorophyll-a and total suspended solids retrieval and mapping using Sentinel-2A and machine learning for inland waters. *Ecol. Indicators* 113.
- Schallenberg, M., de Winton, M.D., Verburg, P., Kelly, D.J., Hamill, K.D., Hamilton, D.P., 2013. Ecosystem services of lakes. In: *Ecosystem services in New Zealand: conditions and trends*. Manaaki Whenua Press, Lincoln, pp. 203–225.
- Shen, M., Duan, H., Cao, Z., Xue, K., Qi, T., Ma, J., Song, X., 2020. Sentinel-3 OLCI observations of water clarity in large lakes in eastern China: Implications for SDG 6.3. 2 evaluation. *Remote Sens. Environ.* 247, 111950.
- Small, C., Nicholls, R.J., 2003. A global analysis of human settlement in coastal zones. *J. Coast. Res.* 584–599.
- Steinmetz, F., Deschamps, P.Y., Ramon, D., 2011. Atmospheric correction in presence of sun glint application to MERIS. *Opt. Express* 19 (10), 9783–9800.
- Sterner, R.W., Keeler, B., Polasky, S., Poudel, R., Rhude, K., Rogers, M., 2020. Ecosystem services of Earth's largest freshwater lakes. *Ecosyst. Serv.* 41, 101046.
- Tan, Z., Cao, Z., Shen, M., Chen, J., Song, Q., Duan, H., 2022. Remote estimation of water clarity and suspended particulate matter in Qinghai Lake from 2001 to 2020 using MODIS images. *Remote Sens. (Basel)* 14 (13), 3094.
- Vanhellemont, Q., 2019. Adaptation of the dark spectrum fitting atmospheric correction for aquatic applications of the Landsat and Sentinel-2 archives. *Remote Sens. Environ.* 225, 175–192.
- Verpoorter, C., Kutser, T., Seekell, D.A., Tranvik, L.J., 2014. A global inventory of lakes based on high-resolution satellite imagery. *Geophys. Res. Lett.* 41 (18), 6396–6402.
- Vundo, A., Matsushita, B., Jiang, D., Gondwe, M., Hamzah, R., Setiawan, F., Fukushima, T., 2019. An overall evaluation of water transparency in Lake Malawi from MERIS data. *Remote Sens. (Basel)* 11 (3), 279.
- Warren, M.A., Simis, S.G., Martinez-Vicente, V., Poser, K., Bresciani, M., Alikas, K., Ansper, A., 2019. Assessment of atmospheric correction algorithms for the Sentinel-2A MultiSpectral Imager over coastal and inland waters. *Remote Sens. Environ.* 225, 267–289.
- Xu, J., Bian, Y., Lyu, H., Miao, S., Li, Y., Liu, H., Xu, J., 2021. Estimation of particulate backscattering coefficient in turbid inland water using Sentinel 3A-OLCI image. *IEEE J. Sel. Top. Appl. Earth Obs. Remote Sens.* 14, 8577–8593.
- Zhang, X., Hu, L., He, M.X., 2009. Scattering by pure seawater: Effect of salinity. *Opt. Express* 17 (7), 5698–5710.